Spin-orbit dependence of anisotropic current-induced spin polarization

L. L. Tao ●* and Evgeny Y. Tsymbal ●†

Department of Physics and Astronomy & Nebraska Center for Materials and Nanoscience,
University of Nebraska, Lincoln, Nebraska 68588, USA

Studies of the current-induced spin polarization (CISP) have been recently reinvigorated due to the discoveries of CISP in some burgeoning materials such as oxide interfaces, van der Waals, and topological quantum materials. Here, we investigate the CISP in two-dimensional systems for different types of spin-orbit coupling (SOC) using the Boltzmann transport theory. We find an anisotropic response of CISP to the current direction which strongly depends on the type of SOC. We demonstrate that the CISP is nonlinear with respect to the SOC magnitude, depends on the Fermi energy, and exhibits two different transport regimes for low or high carrier density. Finally, we propose a magnetoresistance device which can exploit the predicted CISP anisotropy.

I. INTRODUCTION

Current-induced spin polarization (CISP) is a nonequilibrium spin polarization induced in a conductor with spin-orbit coupling (SOC) by passing an electric current [1,2]. Jointly with the anomalous Hall effect (AHE) [3] and the spin Hall effect (SHE) [4,5], the CISP represents a charge-to-spin conversion which is interesting for spintronics [6]. However, unlike the AHE/SHE and tunneling AHE/SHE [7,8] generating spin accumulation at the edges of the conductor, the CISP is spatially homogeneous. The CISP effect was originally proposed by Ivchenko and Pikus [9] for semiconductors lacking space-inversion symmetry. Later, it was theoretically explored in a two-dimensional electron gas (2DEG) with Dresselhaus SOC (DSOC) by Aronov *et al.* [10,11] and Rashba SOC (RSOC) by Edelstein [12]. The latter phenomenon is known as the Edelstein effect. Owing to the spin polarization being generated and controlled in nonmagnetic materials by purely electrical means, the CISP offers promising applications in all-electric spintronic devices [13–17]. Recently, CISP has been experimentally observed in various 2D systems such as a Bi/Ag bilayer [18,19], surface of topological insulator Bi_2Se_3 [20,21], oxide interfaces $LaAlO_3/SrTiO_3$ [22–24], a van der Waals heterostructure [25], and ferroelectric materials [26,27]. In the above systems, the combination of broken inversion symmetry and strong SOC derived from heavy elements results in RSOC, which is critical for generation of CISP.

On the theoretical side, CISP has been extensively studied for 2DEGs [28–34]. For example, Silsbee developed a theoretical model for the detection of CISP via electrical measurements [28]. Trushin and Schliemann investigated the anisotropy of CISP for the 2DEG with RSOC and DSOC in the high-density limiting case [29]. Johansson *et al.* explored

the anisotropy of electron mass and RSOC on the CISP within the semiclassical Boltzmann transport theory [33]. Most of these works, however, focused on RSOC and derived formula for CISP formula up to the linear order in SOC magnitude and under high-density regime approximation. Here, using Boltzmann transport theory, we provide a systematic investigation of anisotropic CISP for different types of SOC and explore the Fermi energy dependence beyond the linear order in SOC approximation. We show that the CISP is highly anisotropic, both in magnitude and direction, and strongly depends on the type of SOC. We demonstrate a very different behavior of the CISP as a function the Fermi energy, depending on the Fermi contour topology.

The rest of the paper is organized as follows. In Sec. II, we describe the Hamiltonian model and present the theoretical formalism and general formula for CISP calculation. In Sec. III, we present the results for spin textures and discuss the topology of the Fermi contours. In Sec. IV, we present the analytical results of CISP for different types of SOC based on the Boltzmann transport theory. Finally, in Sec. IV, we discuss the obtained results and make conclusions.

II. THEORETICAL FORMALISM

We consider a single-particle Hamiltonian describing a 2D system with SOC as follows:

$$H = \frac{\hbar^2 k^2}{2m} + \mathbf{\Omega} \bullet \boldsymbol{\sigma}. \tag{1}$$

Here the first term is the kinetic energy with m being the electron effective mass, $\hbar$ the reduced Planck's constant, and $\mathbf{k} = (k_x, k_y) = k(\cos\phi, \sin\phi)$ the wave vector given in the Cartesian or polar coordinates where ϕ is the azimuthal angle. The second term represents the SOC with $\mathbf{\Omega}$ being the spin-orbit field (SOF) defined in $\mathbf{k}$ space and $\boldsymbol{\sigma} = (\sigma_x, \sigma_y, \sigma_z)$ the Pauli vector. Note that m is assumed to be isotropic in $\mathbf{k}$ space. The eigenvalues $E_{\mathbf{k}s}$ with $s = \pm 1$ being the spin index

*ltao2@unl.edu
†tsymbal@unl.edu

and normalized eigenstates $\psi_{\mathbf{k}s}$ of Hamiltonian (1) take the form

$$E_{\mathbf{k}s} = \frac{\hbar^2 k^2}{2m} + s\Omega \tag{2}$$

and

$$\psi_{\mathbf{k}s} = \frac{e^{i\mathbf{k}\bullet\mathbf{r}}}{\sqrt{2\Omega(\Omega - s\Omega_z)}}\begin{bmatrix}\Omega_x - i\Omega_y\\ s\Omega - \Omega_z\end{bmatrix}, \tag{3}$$

respectively, where $\Omega = \sqrt{\Omega_x^2 + \Omega_y^2 + \Omega_z^2}$. The expectation values of the spin operator can be obtained as

$$\mathbf{s}_{\mathbf{k}s} = \frac{\hbar}{2}\langle\psi_{\mathbf{k}s}|\boldsymbol{\sigma}|\psi_{\mathbf{k}s}\rangle = s\frac{\hbar}{2\Omega}(\Omega_x, \Omega_y, \Omega_z). \tag{4}$$

Being considered as a function of wave vector $\mathbf{k}$, Eq. (4) determines the spin texture in $\mathbf{k}$ space.

At the equilibrium conditions, the system is characterized by the equilibrium Fermi distribution function $f_{\mathbf{k}s}^0$ and the net spin polarization is zero namely $\mathbf{s} = \sum_s \int \mathbf{s}_{\mathbf{k}s} f_{\mathbf{k}s}^0 d\mathbf{k} = 0$. This follows from time-reversal symmetry, which enforces $\mathbf{s}_{\mathbf{k}} = -\mathbf{s}_{-\mathbf{k}}$ and $f_{\mathbf{k}s}^0 = f_{-\mathbf{k}s}^0$. When an external electric field $\boldsymbol{\varepsilon}$ is applied, the Fermi contour in $\mathbf{k}$ space is displaced by $\delta\mathbf{k}$, which is antiparallel to the direction of $\boldsymbol{\varepsilon}$. The magnitude of $\delta\mathbf{k}$ is determined by the collisions of electrons with impurities and phonons [35]. Under the nonequilibrium conditions, time reversal symmetry breaks and the distribution function $f_{\mathbf{k}s}$ deviates from $f_{\mathbf{k}s}^0$, so that $f_{\mathbf{k}s} = f_{\mathbf{k}s}^0 + \delta f_{\mathbf{k}s}$ resulting in the nonzero net spin polarization $\delta\mathbf{s}$ given by

$$\delta\mathbf{s} = \sum_s \int \mathbf{s}_{\mathbf{k}s}\delta f_{\mathbf{k}s}d\mathbf{k}. \tag{5}$$

To obtain $\delta\mathbf{s}$ from Eq. (5), one needs first to calculate $s_{\mathbf{k}s}$ using Eq. (4) and $\delta f_{\mathbf{k}s}$ by solving the Boltzmann transport equation. The latter is generally given by [35]

$$\frac{\partial f_{\mathbf{k}s}^0}{\partial E_{\mathbf{k}s}}(\mathbf{v}_{\mathbf{k}s}\bullet e\boldsymbol{\varepsilon}) = \sum_{\mathbf{k}'s'}(\delta f_{\mathbf{k}s} - \delta f_{\mathbf{k}'s'})Q_{\mathbf{k}'s'}^{\mathbf{k}s}, \tag{6}$$

where $\mathbf{v}_{\mathbf{k}s}$ is the group velocity and $Q_{\mathbf{k}'s'}^{\mathbf{k}s}$ is the scattering probability from state $|\mathbf{k}'s'\rangle$ to state $|\mathbf{k}s\rangle$. According to the Fermi golden rule, $Q_{\mathbf{k}'s'}^{\mathbf{k}s}$ takes the form

$$Q_{\mathbf{k}'s'}^{\mathbf{k}s} = \frac{2\pi}{\hbar}|\langle\mathbf{k}s|V|\mathbf{k}'s'\rangle|^2\delta(E_{\mathbf{k}s} - E_{\mathbf{k}'s'}), \tag{7}$$

where V is an impurity scattering potential. Assuming that the scattering potential is short-ranged, i.e., $V(\mathbf{r}) = V_0\delta(\mathbf{r})$, and using Eq. (3), we arrive at the following equation for $Q_{\mathbf{k}'s'}^{\mathbf{k}s}$:

$$Q_{\mathbf{k}'s'}^{\mathbf{k}s} = \frac{2\pi n V_0^2}{\hbar}[1 + ss'\cos(\gamma_{\mathbf{k}} - \gamma_{\mathbf{k}'})]\delta(E_{\mathbf{k}s} - E_{\mathbf{k}'s'}). \tag{8}$$

Here n is the impurity concentration, $\gamma_{\mathbf{k}} = \tan^{-1}(\Omega_y/\Omega_x)$, and we assume $\Omega_z = 0$. Plugging Eq. (8) into Eq. (6), we obtain

$$\frac{\partial f_{\mathbf{k}s}^0}{\partial E_{\mathbf{k}s}}(\mathbf{v}_{\mathbf{k}s}\bullet e\boldsymbol{\varepsilon}) = \frac{n V_0^2}{2\pi\hbar}\sum_{s'}\int d\mathbf{k}'(\delta f_{\mathbf{k}s} - \delta f_{\mathbf{k}'s'})$$
$$\times [1 + ss'\cos(\gamma_{\mathbf{k}} - \gamma_{\mathbf{k}'})]\delta(E_{\mathbf{k}s} - E_{\mathbf{k}'s'}). \tag{9}$$

TABLE I. The SOFs $\boldsymbol{\Omega}$ and spin textures $\mathbf{s}$ for four different SOC types. α, β, γ and λ are the linear SOC parameters.

SOC	Ω	$\mathbf{s}$ (in $\hbar/2$)
RSOC	$\alpha(-k_y, k_x, 0)$	$\pm(-k_y, k_x, 0)/k$
DSOC	$\beta(k_x, -k_y, 0)$	$\pm(k_x, -k_y, 0)/k$
WSOC	$\gamma(k_x, k_y, 0)$	$\pm(k_x, k_y, 0)/k$
PSOC	$\lambda(k_x - k_y)(1, 1, 0)$	$\pm\mathrm{sgn}(k_x - k_y)(1, 1, 0)/\sqrt{2}$

In the following, we adopt the constant relaxation time approximation, which has been widely used previously [1,28,31,36]. Within such approximation, $\delta f_{\mathbf{k}s} = e\tau(\mathbf{v}_{\mathbf{k}s}\bullet\boldsymbol{\varepsilon})\partial f_{\mathbf{k}s}^0/\partial E_{\mathbf{k}s}$, where τ is the constant relaxation time. In a zero-temperature limit, $-\partial f_{\mathbf{k}s}^0/\partial E_{\mathbf{k}s} = \delta(E_{\mathbf{k}s} - E_F)$, and the integration in Eq. (5) can be carried out over the Fermi contour S_F, namely [31,36]

$$\delta\mathbf{s} = -\frac{e\tau}{(2\pi)^2}\sum_s\int\frac{\mathbf{s}_{\mathbf{k}s}(\mathbf{v}_{\mathbf{k}s}\bullet\boldsymbol{\varepsilon})}{\hbar|\mathbf{v}_{\mathbf{k}s}|}dS_F. \tag{10}$$

Analogously, the current density $\mathbf{j}_e$ is given by [35]

$$\mathbf{j}_e = \frac{e^2\tau}{(2\pi)^2}\sum_s\int\frac{\mathbf{v}_{\mathbf{k}s}(\mathbf{v}_{\mathbf{k}s}\bullet\boldsymbol{\varepsilon})}{\hbar|\mathbf{v}_{\mathbf{k}s}|}dS_F. \tag{11}$$

Since $\delta\mathbf{s}$ is an implicit function of $\mathbf{j}_e$, one can obtain $\delta\mathbf{s}$ as a function of $\mathbf{j}_e$ by combining Eqs. (10) and (11).

III. SPIN TEXTURE AND FERMI CONTOUR TOPOLOGY

Here we consider four different types of SOC, namely RSOC, DSOC, Weyl (WSOC), and persistent-spin-texture (PSOC) types. The corresponding SOFs $\boldsymbol{\Omega}$ and calculated spin textures $\mathbf{s}$ are listed in Table I. Figure 1 shows the schematic plots of the Fermi contours and spin textures when Fermi energy $E_F > 0$. From Eq. (2) and Table I, the energy splitting $E_+ - E_-$ for RSOC, DSOC, and WSOC is proportional to k, indicating the isotropic energy splitting in $\mathbf{k}$ space, as seen from Figs. 1(a), 1(b), and 1(c). While for PSOC, the energy splitting $E_+ - E_-$ is proportional to $k|\cos\phi - \sin\phi|$, indicating that the energy splitting is maximum at $\phi = 3\pi/4$, $7\pi/4$, and zero at $\phi = \pi/4$, $5\pi/4$, as seen from Fig. 1(d). For RSOC, when moving over the Fermi contour, the spin rotates in the same direction as ϕ and is always perpendicular to $\mathbf{k}$. In the case of DSOC, the spin rotates in the opposite direction to ϕ and thus can make any angle to $\mathbf{k}$ depending on ϕ. For WSOC, the spin is ether parallel or antiparallel to $\mathbf{k}$. In the case of PSOC, the spin is unidirectional and thus independent of $\mathbf{k}$. The above different types of SOC appear in realistic materials [37], such as RSOC in 2D materials [38,39], DSOC in ferroelectric HfO_2 [40], WSOC in elemental Te and Se [41,42], and PSOC in $BiInO_3$ [43].

It is noteworthy that the topology of the Fermi contour depends on E_F. Figure 1 assumes that the Fermi energy E_F crosses both energy branches E_+ and E_-, i.e. $E_F > 0$. However, for $E_F < 0$, as shown in Fig. 2(a) for RSOC, DSOC, and WSOC, the E_F crosses only the lower band E_- and the Fermi contour is an annulus. E_F crosses both bands only when $E_F > 0$, where the Fermi contour evolves into two circles [Fig. 2(b)]. In the case of PSOC, for $E_F < 0$,
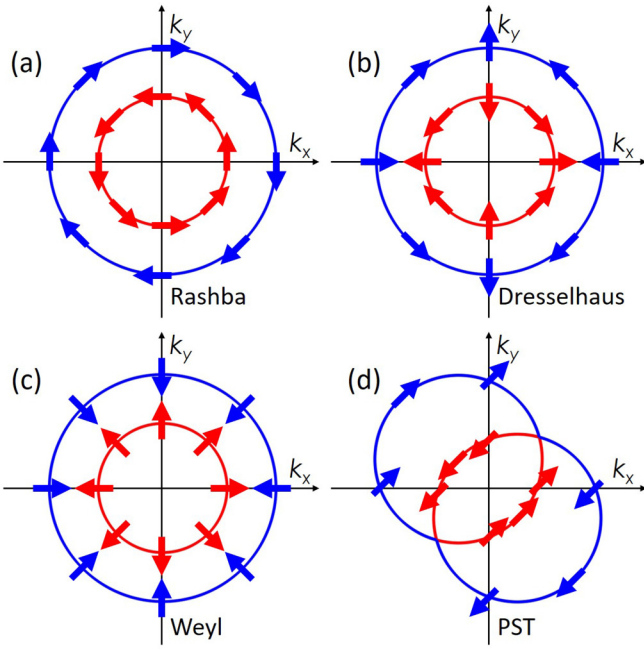
FIG. 1. Schematic Fermi contours ($E_F > 0$ case) and spin textures for (a) RSOC, (b) DSOC, (c) WSOC, and (d) PSOC. Arrows indicate the spin directions while the red and blue contour lines represent the E_+ and E_- energy branches, respectively.
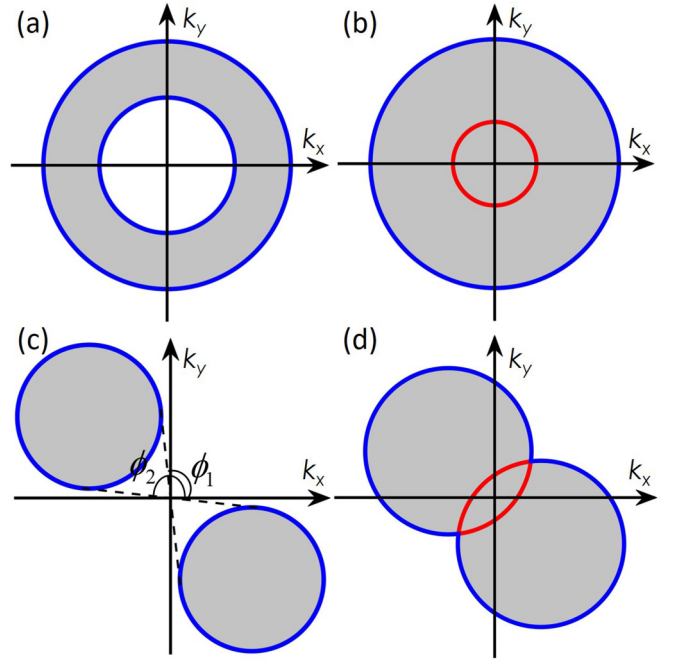

FIG. 2. Schematic Fermi contours for (a), (b) RSOC, DSOC or WSOC and (c), (d) PSOC. (a), (c) for $E_F < 0$, and (b), (d) for $E_F > 0$. The gray shaded regions represent the electron occupied states. In (c), $\phi_{1,2}$ ($\phi_1 + \phi_2 = 3\pi/2$) denotes the critical angles separating the electron occupied and unoccupied states. Red and blue contour lines represent the E_+ and E_- energy branches, respectively.

the E_F crosses only the lower band E_- and the Fermi contours are two well-separated circles centered at wave vectors $m\alpha/\hbar^2(-\sqrt{2}, \sqrt{2})$ and $m\alpha/\hbar^2(\sqrt{2}, -\sqrt{2})$, which are E_F independent [Fig. 2(c)]. For $E_F > 0$, the E_F crosses both E_+ and E_-, and the Fermi contour is characterized by two intersecting circles centered at $\sqrt{2m^2\alpha^2 + mE_F}/\hbar(-1, 1)$ and $\sqrt{2m^2\alpha^2 + mE_F}/\hbar(1, -1)$, which are E_F dependent. We see that the topology of the Fermi contour changes as E_F varies, and there is a topological transition point at $E_F = 0$. As we will demonstrate in the following sections, the topology of the Fermi contour strongly affects the CISP.

IV. CURRENT-INDUCED SPIN POLARIZARION

In this section, we derive the expressions for CISP for four different types of SOC. The electric field is assumed to have the form $\boldsymbol{\varepsilon} = \varepsilon(\cos\varphi, \sin\varphi)$, where φ is the azimuthal angle in the polar coordinate system.

A. Rashba type

From Eq. (2) and Table I, the eigenvalue E_s for RSOC is given by $E_s = \hbar^2(k + sk_R)^2/(2m) - E_R$, where $k_R = m\alpha/\hbar^2$ and $E_R = m\alpha^2/(2\hbar^2)$. Accordingly, the group velocity can be calculated as $\mathbf{v}_s = \hbar\mathbf{k}/m + s\alpha\mathbf{k}/(\hbar k)$. From $E_s = E_F$, we obtain the Fermi wave vector as follows:

$$k_{F\eta} = k_R - \eta\sqrt{k_R^2 - k_0^2}, \quad E_c < E_F \leqslant 0$$

$$k_{Fs} = \sqrt{k_R^2 + k_0^2} - sk_R, \quad E_F > 0, \qquad (12)$$

where $\eta = \pm 1$, $E_c = -E_R$ denotes the band minimum and $k_0 = \sqrt{2m|E_F|/\hbar^2}$.

When $E_c < E_F \leqslant 0$, from Eqs. (10) and (11), $\delta\mathbf{s}$ is calculated as

$$
\delta\mathbf{s} = \sum_\eta \frac{e\varepsilon\tau}{8\pi^2} \int_0^{2\pi} \begin{pmatrix} -\sin\phi \\ \cos\phi \end{pmatrix} \cos(\phi - \varphi)(-\eta k_{F\eta})d\phi
$$
$$
= \frac{e\varepsilon\tau\sqrt{2m(E_F + E_R)}}{4\pi\hbar} \begin{pmatrix} -\sin\varphi \\ \cos\varphi \end{pmatrix}, \qquad (13)
$$

and $\mathbf{j}_e$ is calculated as

$$
\mathbf{j}_e = \sum_\eta \frac{e^2\tau\boldsymbol{\varepsilon}}{4\pi^2\hbar} \int_0^{2\pi} \left| \frac{\hbar k_{F\eta}}{m} - \frac{\alpha}{\hbar} \right| k_{F\eta}\cos^2(\phi - \varphi)d\phi
$$
$$
= \frac{e^2\tau\boldsymbol{\varepsilon}}{\pi\hbar^2}\sqrt{E_R(E_F + E_R)}. \qquad (14)
$$

When $E_F > 0$, in a similar way, $\delta\mathbf{s}$ is calculated as

$$
\delta\mathbf{s} = -\sum_s \frac{e\varepsilon\tau}{8\pi^2} \int_0^{2\pi} \begin{pmatrix} -\sin\phi \\ \cos\phi \end{pmatrix} \cos(\phi - \varphi)sk_{Fs}d\phi
$$
$$
= \frac{e\varepsilon\tau\sqrt{2mE_R}}{4\pi\hbar} \begin{pmatrix} -\sin\varphi \\ \cos\varphi \end{pmatrix}, \qquad (15)
$$

and $\mathbf{j}_e$ is calculated as

$$
\mathbf{j}_e = \sum_s \frac{e^2\tau\boldsymbol{\varepsilon}}{4\pi^2\hbar} \int_0^{2\pi} \frac{\hbar}{m}\sqrt{k_R^2 + k_0^2}\,k_{Fs}\cos^2(\phi - \varphi)d\phi
$$
$$
= \frac{e^2\tau\boldsymbol{\varepsilon}}{\pi\hbar^2}(E_F + E_R). \qquad (16)
$$

Thus, $\delta\mathbf{s}$ as a function of j_e and E_F for RSOC is given by

$$
\delta\mathbf{s} = \begin{cases} \dfrac{\sqrt{2m}\hbar j_e}{4e\sqrt{E_R}}\begin{pmatrix} -\sin\varphi \\ \cos\varphi \end{pmatrix}, & E_c < E_F \leqslant 0 \\[3mm] \dfrac{\sqrt{2mE_R}\hbar j_e}{4e(E_F+E_R)}\begin{pmatrix} -\sin\varphi \\ \cos\varphi \end{pmatrix}, & E_F > 0 \end{cases}. \quad (17)
$$

In the high-density regime, i.e., when $E_F \gg E_R$, $\delta\mathbf{s}$ becomes linearly dependent on the RSOC parameter α, which is consistent with the previous work [30–32]. In general, however, $\delta\mathbf{s}$ is a nonlinear function of α. Moreover, as follows from Eq. (17), $\delta\mathbf{s}$ is inversely proportional to α in the low density regime when $E_c < E_F \leqslant 0$. It is noteworthy that the relaxation time τ is assumed to be spin dependent in some previous works [1,28,31], namely $\tau_s = \tau(1-sk_R/k_0)$ up to linear order in α when $E_F \gg E_R$. Taking this into account, $\delta\mathbf{s}$ will be modified accordingly as

$$
\delta\mathbf{s} = \frac{e\varepsilon\tau\sqrt{2mE_R}}{4\pi\hbar}\left(1+\sqrt{1+\frac{E_R}{E_F}}\right)\begin{pmatrix} -\sin\varphi \\ \cos\varphi \end{pmatrix}, \quad (18)
$$

and $\mathbf{j}_e$ is

$$
\mathbf{j}_e = \frac{e^2\tau\boldsymbol{\varepsilon}}{\pi\hbar^2}\left[E_F + E_R\left(1+\sqrt{1+\frac{E_R}{E_F}}\right)\right]. \quad (19)
$$

Eqation (17) is thus modified as

$$
\delta\mathbf{s} = \begin{cases} \dfrac{\sqrt{2m}\hbar j_e}{4e\sqrt{E_R}}\begin{pmatrix} -\sin\varphi \\ \cos\varphi \end{pmatrix}, & E_c < E_F \leqslant 0 \\[3mm] \dfrac{\sqrt{2mE_R}\hbar j_e}{2e(E_F+2E_R)}\begin{pmatrix} -\sin\varphi \\ \cos\varphi \end{pmatrix}, & E_F > 0 \end{cases}. \quad (20)
$$

It is seen that there is a factor of 2 difference when $E_F \gg E_R$ between Eqs. (17) and (20), which is in line with previous work [31]. On the other hand, as seen from Eqs. (13) and (15) describing ε dependence of δs and Eq. (17) describing j_e dependence of δs, the E_R dependence of δs is completely different for a constant-voltage experiment and a constant-current experiment. For the former, $\delta s \sim \sqrt{E_F + E_R}$ when $E_c < E_F \leqslant 0$ and $\delta s \sim \sqrt{E_R}$ when $E_F > 0$. For the later, $\delta s \sim 1/\sqrt{E_R}$ when $E_c < E_F \leqslant 0$ and $\delta s \sim \sqrt{E_R}/(E_F + E_R)$ when $E_F > 0$.

B. Dresselhaus type

For DSOC, the eigenvalue E_s is given by $E_s = \hbar^2(k+sk_D)^2/(2m) - E_D$, where $k_D = m\beta/\hbar^2$ and $E_D = m\beta^2/(2\hbar^2)$. In a similar way as in Sec. IV A above, we obtain for $\delta\mathbf{s}$ a function of j_e and E_F:

$$
\delta\mathbf{s} = \begin{cases} \dfrac{\sqrt{2m}\hbar j_e}{4e\sqrt{E_D}}\begin{pmatrix} \cos\varphi \\ -\sin\varphi \end{pmatrix}, & E_c < E_F \leqslant 0 \\[3mm] \dfrac{\sqrt{2mE_D}\hbar j_e}{4e(E_F+E_D)}\begin{pmatrix} \cos\varphi \\ -\sin\varphi \end{pmatrix}, & E_F > 0 \end{cases}, \quad (21)
$$

where $E_c = -E_D$ denotes the band minimum.

C. Weyl type

For WSOC, the eigenvalue E_s is given by $E_s = \hbar^2(k+sk_W)^2/(2m) - E_W$, where $k_W = m\gamma/\hbar^2$ and $E_W = m\gamma^2/(2\hbar^2)$.

Using a similar calculation, we obtain for $\delta\mathbf{s}$ a function of j_e and E_F:

$$
\delta\mathbf{s} = \begin{cases} \dfrac{\sqrt{2m}\hbar j_e}{4e\sqrt{E_W}}\begin{pmatrix} \cos\varphi \\ \sin\varphi \end{pmatrix}, & E_c < E_F \leqslant 0 \\[3mm] \dfrac{\sqrt{2mE_W}\hbar j_e}{4e(E_F+E_W)}\begin{pmatrix} \cos\varphi \\ \sin\varphi \end{pmatrix}, & E_F > 0 \end{cases}, \quad (22)
$$

where $E_c = -E_W$ denotes the band minimum.

D. PST type

For PSOC, the eigenvalue E_s is given by $E_s = \hbar^2(k+sk_\phi)^2/(2m) - E_\phi$, where $k_\phi = \sqrt{2}m\lambda|\cos\phi - \sin\phi|/\hbar^2$ and $E_\phi = m\lambda^2(\cos\phi - \sin\phi)^2/\hbar^2$. Accordingly, the group velocity is calculated as $\mathbf{v}_s = \hbar\mathbf{k}/m + s\sqrt{2}\lambda/\hbar\,\mathrm{sgn}(\cos\phi - \sin\phi)(1,-1)$. From $E_s = E_F$, we obtain for the Fermi wave vector

$$
k_{F\eta} = k_\phi - \eta\sqrt{k_\phi^2 - k_0^2}, \quad E_c < E_F \leqslant 0
$$

$$
k_{Fs} = \sqrt{k_\phi^2 + k_0^2} - sk_\phi, \quad E_F > 0, \quad (23)
$$

where $E_c = -2m\lambda^2/\hbar^2 = -E_P$ denotes the band minimum.

When $E_c < E_F \leqslant 0$, $\delta\mathbf{s}$ can be calculated as

$$
\delta\mathbf{s} = \frac{e\varepsilon\tau\sqrt{m}(E_F+E_P)}{3\sqrt{2}\pi^2\hbar\sqrt{E_P}}(\cos\varphi - \sin\varphi)\begin{pmatrix} 1 \\ 1 \end{pmatrix}, \quad (24)
$$

and $\mathbf{j}_e$ is calculated as

$$
\mathbf{j}_e = \frac{e^2\tau\boldsymbol{\varepsilon}}{\pi^2\hbar^2}\left[2(E_F+E_P) + \left(\frac{14}{15}E_F + \frac{2}{15}E_P + \frac{4E_F^2}{5E_P}\right)\sin 2\varphi\right]. \quad (25)
$$

For $E_F > 0$, analytic expressions for $\delta\mathbf{s}$ and $\mathbf{j}_e$ can be obtained within the high-density regime assumption, i.e., $E_F \gg E_P$. For $\delta\mathbf{s}$ we find

$$
\delta\mathbf{s} = \frac{e\varepsilon\tau\sqrt{m}(E_P)^{3/2}}{16\sqrt{2}\pi\hbar\sqrt{E_F(E_F+E_P)}}(\cos\varphi - \sin\varphi)\begin{pmatrix} 1 \\ 1 \end{pmatrix}, \quad (26)
$$

and for $\mathbf{j}_e$ we find

$$
\mathbf{j}_e = \frac{e^2\tau\boldsymbol{\varepsilon}}{4\pi\hbar^2\sqrt{E_F+E_P}}\left[4E_F\sqrt{E_F} + 5E_P\sqrt{E_F} - \frac{2E_P^2}{\sqrt{E_F}} + \left(\frac{2E_P^2}{\sqrt{E_F}} - \frac{E_P\sqrt{E_F}}{2}\right)\sin 2\varphi\right]. \quad (27)
$$

Details of the derivation of Eqs. (24)–(27) are presented in the Appendix. Noteworthy is the fact that, although the analytic expressions given by Eqs. (26) and (27) are derived within the high-density regime, the φ dependent functional relationships $\delta\mathbf{s} \sim (\cos\varphi - \sin\varphi)$ and $\mathbf{j}_e \sim \sin 2\varphi$ hold exactly, as seen from Eqs. (A3) and (A4).

Figure 3 shows $\delta\mathbf{s}$ as a function of φ including magnitude δs (blue lines) and direction (red arrows). For RSOC, DSOC, and WSOC, shown in Figs. 3(a)–3(c), from Eqs. (17), (21), and (22), we see that δs is φ independent, indicating that δs is isotropic. However, the direction of $\delta\mathbf{s}$ is strongly φ dependent. In fact, the $\delta\mathbf{s}$ orientation mirrors the spin textures
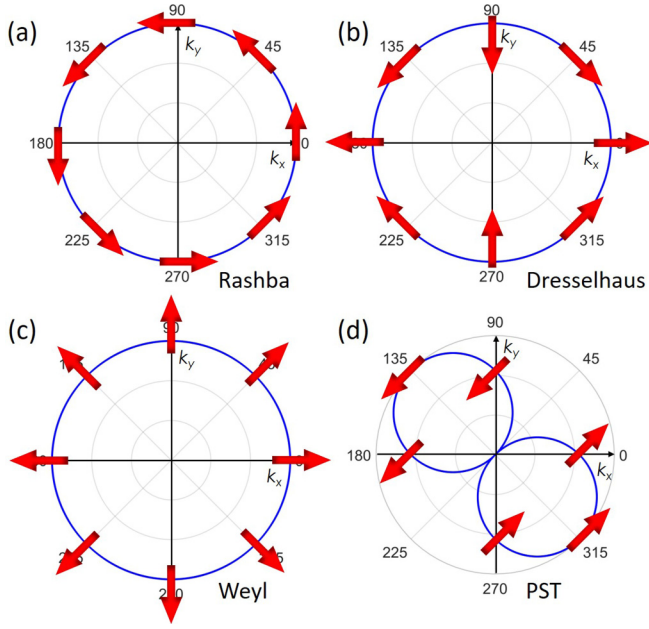
FIG. 3. $\delta \mathbf{s}$ as a function of the direction of the electric field φ in polar coordinates for (a) RSOC, (b) DSOC, (c) WSOC and (d) PSOC. Blue lines represent the magnitude while the red arrows indicate the direction of $\delta \mathbf{s}$.
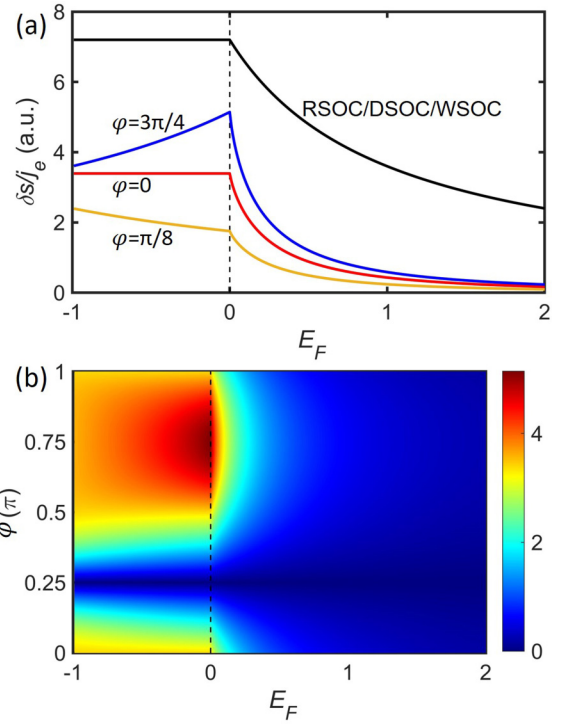

FIG. 4. (a) CISP efficiency $\delta s / j_e$ as a function of E_F (in units of $|E_c|$) for RSOC, DSOC, and WSOC (black line) and PSOC when $\varphi = 0$ (red line), $\varphi = \pi/8$ (orange line) and $\varphi = 3\pi/4$ (blue line). (b) CISP efficiency $\delta s / j_e$ (color) as a function of E_F and the direction of the electric field φ for PSOC. The SOC parameters are assumed to be $\alpha = \beta = \gamma = 2\lambda = 1.0$ eV Å and electron effective mass is $m = 0.5$, under which the band minima E_c are the same for the different types of SOC. The vertical dashed lines indicate the topological transition point of the Fermi contour.

shown in Figs. 1(a)–1(c) (the inner branches indicated by red lines). In the case of PSOC, from Eqs. (24) and (26), δs as a function of φ is determined by $|cos \varphi - sin \varphi|$, indicating perfect anisotropy of δs, so that δs is zero at $\varphi = \pi/4$, $5\pi/4$ and δs is maximum at $\varphi = 3\pi/4$, $7\pi/4$. Like for the other types of SOC, the direction of $\delta \mathbf{s}$ for PSOC mirrors the spin texture [Fig. 1(d)], the inner branch indicated by red line).

Figure 4(a) shows the E_F dependence of the CISP efficiency $\delta s / j_e$, which is defined as the ratio of the magnitudes of $\delta \mathbf{s}$ and $\mathbf{j}_e$. For PSOC and the energy range of $E_F > 0$, $\delta s / j_e$ is obtained using numerical calculations. As seen from Fig. 4(a), in the case of RSOC, DSOC, and WSOC, when $E_c < E_F \leqslant 0$, $\delta s / j_e$ is a constant. When $E_F > 0$, $\delta s / j_e$ decreases monotonically as E_F increases, consistent with Eqs. (17)–(22). Similar behavior was also observed in the graphene on a transition metal dichalcogenide monolayer with combination of RSOC and Zeeman SOC [44].

Such a dissimilar behavior of $\delta s / j_e$ versus E_F can be understood from the analysis the Fermi contour topology. Taking RSOC as an example, we see from Fig. 2(a) that for $E_c < E_F \leqslant 0$, the Fermi surface represents two SOC-split concentric circles with the *same* spin configurations. As a result, both δs and j_e are proportional to the sum of the their perimeters, which according to Eq. (12) is proportional to $\sqrt{E_F + E_R}$. This yields the same E_F dependence of δs and j_e, i.e. $\delta s \sim j_e \sim \sqrt{E_F + E_R}$, and hence the constant $\delta s / j_e$. On the contrary, when $E_F > 0$, as seen from Fig. 2(b), the two SOC-split concentric Fermi circles have *opposite* spin configurations. As a result, while j_e is still proportional to the sum of the circumferences, δs is proportional to their difference. This leads to the different E_F dependence of δs and j_e, which according to Eq. (12) is given by $\delta s \sim \sqrt{E_R}$ and

$j_e \sim \sqrt{E_F + E_R}$, resulting in $\delta s / j_e \sim 1/\sqrt{E_F + E_R}$. The same argument applies to DSOC and WSOC.

In the case of PSOC, the two Fermi contours do not represent concentric circles [Figs. 2(c) and 2(d)] and the behavior of $\delta s / j_e$ as a function of E_F is more complicated. As seen from Fig. 4(a), when $\varphi = 0$ (red line), $\delta s / j_e$ is a constant in the energy range $E_c < E_F \leqslant 0$ and decreases monotonically when $E_F > 0$, consistent with Eqs. (24) and (25). When $\varphi = 3\pi/4$ (blue line), $\delta s / j_e$ increases (decreases) monotonically in the range $E_c < E_F \leqslant 0$ ($E_F > 0$) as E_F increases, indicating that $\delta s / j_e$ reaches maximum at the transition point $E_F = 0$. When $\varphi = \pi/8$ (orange line), $\delta s / j_e$ decreases monotonically in the whole energy range. Fig. 4(b) shows the $\delta s / j_e$ for PSOC as a function of E_F and electrical field direction φ (with period π). It is seen that the optimal condition, at which $\delta s / j_e$ reaches maximum, appears at $E_F = 0$ and $\varphi = 3\pi/4$.

Figure 5 shows the CISP efficiency $\delta s / j_e$ as a function of SOC parameters. In the case of RSOC, DSOC, and WSOC shown in Fig. 5(a), when $E_c < E_F \leqslant 0$, $\delta s / j_e$ decreases monotonically as α increases due to $\delta s / j_e \sim 1/\alpha$ as seen from Eq. (17). When $E_F > 0$, $\delta s / j_e$ becomes maximum at the critical point $\alpha = \hbar \sqrt{2E_F/m}$, as obtained from Eq. (17). In the case of PSOC shown in Fig. 5(b), the λ dependency of $\delta s / j_e$ shows qualitatively similar behavior.
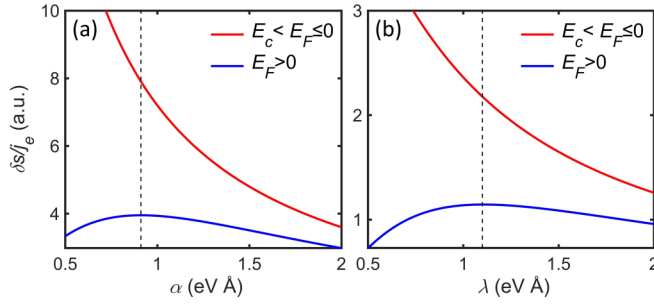
FIG. 5. CISP efficiency $\delta s/j_e$ as a function of SOC parameters α and λ for (a) RSOC/DSOC/WSOC type and (b) PSOC type. The other parameters are assumed to be $m = 0.5$, $|E_F| = 27.2$ meV and $\varphi = 3\pi/4$ in (b). The dashed lines denote the critical points, at which $\delta s/j_e$ reaches maximum when $E_F > 0$.

V. DISCUSSION AND CONCLUSIONS

We would like to emphasize the different dependence of the CISP efficiency on the Fermi energy below and above the topological transition point. For RSOC, the CISP efficiency is higher below the transition point than that above the transition point. This follows from reversal of the spin texture at the inner Fermi contour which enhances the induced spin polarization below the transition point due to parallel spin directions on the two SOC-split Fermi contours.

In this low carrier density regime, i.e., when $E_c < E_F \leqslant 0$, the CISP is inversely proportional to α [Eq. (17)], which seems to be counterintuitive. However, one should take into account the fact that reducing α implies, for a given E_F, reducing j_e [Eq. (14)] due to the reduced carrier density. From Eq. (12), the electron density n can be calculated as

$$n(E_F) = \begin{cases} 2N_0\sqrt{E_R(E_F + E_R)}, & E_c < E_F \leqslant 0 \\ N_0(E_F + 2E_R), & E_F > 0 \end{cases}, \quad (28)$$

where $N_0 = m/(\pi\hbar^2)$ is the density of states for a free 2DEG. The critical density at the transition point $E_F = 0$ is $n_0 = m^2\alpha^2/(\pi\hbar^4)$, which depends quadratically on the RSOC parameter α.

We estimate the critical carrier density n_0 for realistic systems. For a LaAlO$_3$/SrTiO$_3$ 2DEG, the Rashba parameter α ranges from 0.015 to 0.043 eV Å [45], $m = 0.4\,m_0$, and we obtain n_0 varying from 2.0×10^9 cm^{-2} to 1.6×10^{10} cm^{-2}. These values of n_0 are much smaller than the typical carrier density of the 2DEG varying from $\sim 1 \times 10^{13}$ to $\sim 1 \times 10^{14}$ cm^{-2}. Therefore, the high carry density regime is well justified for a LaAlO$_3$/SrTiO$_3$ 2DEG.

The situation is, however, very different for a Bi/Ag system [19], where $\alpha = 3.05$ eV Å, $m = 0.35\,m_0$, and therefore $n_0 \approx 6.2 \times 10^{13}$ cm^{-2}. The measured electron density is in the range from 0.5×10^{13} to 4.0×10^{13} cm^{-2}, which is less than the critical carrier density. This corresponds to the low carrier density regime, where an "anomalous" behavior of the CISP is expected. It would be interesting to experimentally verify the validity of Eq. (17) by investigating the CISP efficiency for a Bi/Ag system with varying carrier concentration.

In this work, we limit our investigation to SOC linear in k and the higher order contributions are neglected, which is appropriate for the description of systems with C_{2v} and C_{4v} point symmetries [46]. However, for the system with C_{3v} point symmetry [47], the cubic order correction to CISP is also important and needs to be taken into consideration [48]. Second, the electron effective mass in Eq. (1) is assumed to be isotropic in **k** space. In realistic materials, the effective mass is expected to be **k**-direction dependent. It would be thus interesting to explore the effect of mass anisotropy on CISP in the future study. Third, we calculate the CISP based on the constant relaxation time approximation. In general, the scattering probability is spin and wave-vector dependent. It would be therefore desirable to investigate the CISP beyond the constant relaxation time approximation. It is also to be noted that the vertex corrections are neglected in the relaxation time approximation [49] and the vertex corrections could lead to quantitative changes of CISP, but it will not alter our main results qualitatively. Furthermore, the SOC effect due to the electron scattering with random potential is ignored in this work. The effect of spin-orbit scattering has been theoretically investigated by previous work [34]. Fourth, we limit our study to the nonmagnetic systems, where the exchange coupling between conduction electron spin and local magnetization is absent. However, CISP can also be induced in magnetic systems with SOC [50]. The interaction between CISP and local magnetization results in a spin torque on the local magnetization [36,51,52]. In addition, the CISP is expected to be dependent on the magnetization orientation due to the magnetically controlled Fermi contours [53–55]. Lastly, a giant SOC has been demonstrated in certain three-dimensional (3D) bulk systems, such as polar semiconductor BiTeI [56] and ferroelectric crystals [57–59]. Some of these 3D systems exhibit giant SOC, orders of magnitude larger than that in conventional semiconductors, which favors the enhancement of CISP [31]. Besides the SOC magnitude, the spin-torque efficiency, which is defined as the spin torque divided by the current density, is enhanced in 3D systems with RSOC and exchange interaction as compared to 2D systems [60]. It is thus interesting to explore the effect of dimensionality on the CISP efficiency. Finally, the switchable SOC parameters in ferroelectrics by electrically controlled polarization [40,57–59] enables the nonvolatile electric control of CISP.

In summary, we have investigated the anisotropic CISP in two dimensions with different types of SOC using the Boltz-
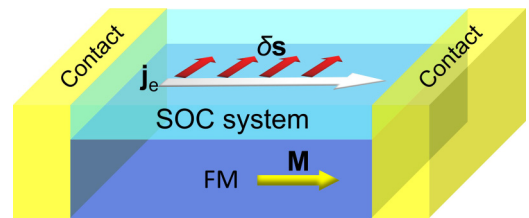

FIG. 6. Schematic illustration of magnetoresistance device due to the interplay of current-direction ($\mathbf{j}_e$, white arrow) dependent CISP $\boldsymbol{\delta s}$ (red arrow) in SOC conductor layer and local magnetization **M** (yellow arrow) in ferromagnetic (FM) layer.

mann transport theory. We demonstrated the strong spatial anisotropy of CISP in terms of direction as well as magnitude. Additionally, we showed the CISP efficiency behaves differently as a function of the Fermi energy below and above the topological transition point of the Fermi contour. The anisotropy of CISP can be further used to explore the spin-dependent transport properties. For example, the electrical conductivity of a bilayer system, which consists of a conducting layer with SOC and ferromagnetic metal layer, is expected to depend on the current direction, as schematically shown in Fig. 6. Such a magnetoresistance effect arises from the interplay between current-direction dependent CISP and local magnetization, as has been recently reported in ferromagnet/heavy metal bilayers [61] and magnetic topological insulator based heterostructures [62,63]. Conversely, measuring the current direction dependent magnetoresistance offers an efficient way to quantify the type of SOC.

APPENDIX: DERIVATION OF EQS. (24)–(27)

From Eq. (10), when $E_c < E_F \leqslant 0$, $\delta\mathbf{s}$ can be calculated as

$$
\begin{aligned}
\delta\mathbf{s} &= \sum_\eta \frac{e\varepsilon\tau}{8\sqrt{2}\pi^2}\begin{pmatrix}1\\1\end{pmatrix}\int_0^{2\pi}\operatorname{sgn}(\cos\phi-\sin\phi)(\hat{v}_k\bullet\hat{\varepsilon})k_{F\eta}d\phi \\
&= \frac{\sqrt{m}e\varepsilon\tau}{8\pi^2\sqrt{E_F+E_P}}\begin{pmatrix}1\\1\end{pmatrix}\int_0^{2\pi}\operatorname{sgn}(\cos\phi-\sin\phi)\left[\left(\frac{2m\lambda^2}{\hbar^3}(1-2\sin2\phi)-\frac{\hbar k_0^2}{m}\right)\cos(\phi-\varphi)+\frac{2m\lambda^2}{\hbar^3}\sin(\phi+\varphi)\right]d\phi \\
&= -\frac{\sqrt{m}e\varepsilon\tau}{4\pi^2\sqrt{E_F+E_P}}\begin{pmatrix}1\\1\end{pmatrix}\int_{\phi_1}^{\phi_2}\left[\left(\frac{2m\lambda^2}{\hbar^3}(1-2\sin2\phi)-\frac{\hbar k_0^2}{m}\right)\cos(\phi-\varphi)+\frac{2m\lambda^2}{\hbar^3}\sin(\phi+\varphi)\right]d\phi \\
&= -\frac{\sqrt{m}e\varepsilon\tau}{4\pi^2\sqrt{E_F+E_P}}\begin{pmatrix}1\\1\end{pmatrix}\left[\frac{\hbar k_0^2}{m}(\cos\phi_1-\cos\phi_2)-\frac{8m\lambda^2}{3\hbar^3}(\cos^3\phi_1-\cos^3\phi_2)\right](\cos\varphi-\sin\varphi) \\
&= \frac{e\varepsilon\tau\sqrt{m}(E_F+E_P)}{3\sqrt{2}\pi^2\hbar\sqrt{E_P}}(\cos\varphi-\sin\varphi)\begin{pmatrix}1\\1\end{pmatrix},
\end{aligned}
\tag{A1}
$$

where the critical angles $\phi_{1,2}$ [see Fig. 2(c)] are given by $\phi_{1,2} = \sin^{-1}(\frac{\sqrt{2}\hbar^2 k_0}{4m\lambda}\pm\sqrt{\frac{1}{2}-\frac{\hbar^4 k_0^2}{8m^2\lambda^2}})$, as obtained from $|k_\phi| = |k_0|$. From Eq. (11), the current density $\mathbf{j}_e$ is calculated as

$$
\begin{aligned}
\mathbf{j}_e &= \sum_\eta\frac{e^2\tau\boldsymbol{\varepsilon}}{4\pi^2\hbar}\int_0^{2\pi}|v_{F\eta}|(\hat{v}_k\bullet\hat{\varepsilon})^2 k_{F\eta}d\phi \\
&= \frac{\sqrt{m}e^2\tau\boldsymbol{\varepsilon}}{2\sqrt{2}\pi^2\hbar\sqrt{E_F+E_P}}\sum_\eta\int_{\phi_1}^{\phi_2}\left[\frac{\hbar^2 k_{F\eta}^3}{m^2}(\cos^2\phi\cos^2\varphi+\sin^2\phi\sin^2\varphi)+\frac{2\sqrt{2}\lambda k_{F\eta}^2}{m}(\cos\phi\cos^2\varphi-\sin\phi\sin^2\varphi)\right. \\
&\qquad\left.+\frac{2\lambda^2 k_{F\eta}}{\hbar^2}+\frac{\hbar^2 k_{F\eta}^3}{2m^2}\sin2\phi\sin2\varphi-\frac{2\lambda^2 k_{F\eta}}{\hbar^2}\sin2\varphi+\frac{\sqrt{2}\lambda k_{F\eta}^2}{m}(\sin\phi-\cos\phi)\sin2\varphi\right]d\phi \\
&= \frac{\sqrt{m}e^2\tau\boldsymbol{\varepsilon}}{\sqrt{2}\pi^2\hbar\sqrt{E_F+E_P}}\int_{\phi_1}^{\phi_2}\left[\frac{\hbar^2}{m^2}(4k_\phi^3-3k_\phi k_0^2)\cos^2\phi+\frac{2\sqrt{2}\lambda}{m}(2k_\phi^2-k_0^2)\cos\phi+\frac{2\lambda^2 k_\phi}{\hbar^2}\right. \\
&\qquad\left.+\frac{\hbar^2}{2m^2}(4k_\phi^3-3k_\phi k_0^2)\sin2\phi\sin2\varphi-\frac{2\lambda^2 k_\phi}{\hbar^2}\sin2\varphi-\frac{2\sqrt{2}\lambda}{m}(2k_\phi^2-k_0^2)\cos\phi\sin2\varphi\right]d\phi \\
&= \frac{e^2\tau\boldsymbol{\varepsilon}}{\pi^2\hbar^2}\left[2(E_F+E_P)+\left(\frac{14}{15}E_F+\frac{2}{15}E_P+\frac{4E_F^2}{5E_P}\right)\sin2\varphi\right].
\end{aligned}
\tag{A2}
$$

When $E_F > 0$, $\delta\mathbf{s}$ can be calculated as

$$
\begin{aligned}
\delta\mathbf{s} &= -\frac{e\varepsilon\tau}{8\sqrt{2}\pi^2}\begin{pmatrix}1\\1\end{pmatrix}\sum_s\int_0^{2\pi}\operatorname{sgn}(\cos\phi-\sin\phi)(\hat{v}_{ks}\bullet\hat{\varepsilon})sk_{Fs}d\phi \\
&= \frac{\sqrt{m}e\varepsilon\tau\lambda}{4\sqrt{2}\pi^2\hbar\sqrt{E_F+E_P}}\begin{pmatrix}1\\1\end{pmatrix}\int_0^{2\pi}[2(\cos\phi-\sin\phi)\cos(\phi-\varphi)-(\cos\varphi-\sin\varphi)]\sqrt{k_\phi^2+k_0^2}d\phi
\end{aligned}
$$

$$
\begin{aligned}
&= -\frac{\sqrt{m}e\varepsilon\tau\lambda}{4\sqrt{2}\pi^2\hbar\sqrt{E_F+E_P}}(\cos\varphi-\sin\varphi)\binom{1}{1}\int_0^{2\pi}\sin 2\phi\sqrt{k_\phi^2+k_0^2}\,d\phi \\
&\approx -\frac{\sqrt{m}e\varepsilon\tau\lambda}{4\sqrt{2}\pi^2\hbar\sqrt{E_F+E_P}}(\cos\varphi-\sin\varphi)\binom{1}{1}\int_0^{2\pi}\sin 2\phi\left(k_0+\frac{k_\phi^2}{2k_0}\right)d\phi \\
&= \frac{e\varepsilon\tau\sqrt{m}(E_P)^{3/2}}{16\sqrt{2}\pi\hbar\sqrt{E_F(E_F+E_P)}}(\cos\varphi-\sin\varphi)\binom{1}{1},
\end{aligned}
\tag{A3}
$$

and $\mathbf{j}_e$ is calculated as

$$
\begin{aligned}
\mathbf{j}_e &= \sum_s \frac{e^2\tau\boldsymbol{\varepsilon}}{4\pi^2\hbar}\int_0^{2\pi}|v_{ks}|(\hat{v}_{ks}\bullet\hat{\varepsilon})^2 k_{Fs}\,d\phi \\
&= \frac{\sqrt{m}e^2\tau\boldsymbol{\varepsilon}}{4\sqrt{2}\pi^2\hbar\sqrt{E_F+E_P}}\sum_s\int_0^{2\pi}\left[\frac{\hbar^2 k_{Fs}^3}{m^2}\cos^2\phi+s\frac{2\sqrt{2}\lambda k_{Fs}^2}{m}\mathrm{sgn}(\cos\phi-\sin\phi)\cos\phi+\frac{2\lambda^2 k_{Fs}}{\hbar^2}\right. \\
&\qquad\qquad \left. +\frac{\hbar^2 k_{Fs}^3}{2m^2}\sin 2\phi\sin 2\varphi-\frac{2\lambda^2 k_{Fs}}{\hbar^2}\sin 2\varphi-s\frac{\sqrt{2}\lambda k_{Fs}^2}{m}|\cos\phi-\sin\phi|\sin 2\varphi\right]d\phi \\
&= \frac{\sqrt{m}e^2\tau\boldsymbol{\varepsilon}}{2\sqrt{2}\pi^2\hbar\sqrt{E_F+E_P}}\int_0^{2\pi}\left[\frac{\hbar^2\sqrt{k_\phi^2+k_0^2}}{m^2}\left(4k_\phi^2+k_0^2-\frac{8m^2\lambda^2}{\hbar^4}\right)\cos^2\phi+\frac{4\lambda^2\sqrt{k_\phi^2+k_0^2}}{\hbar^2}\sin 2\phi\right. \\
&\qquad\qquad \left. +\frac{2\lambda^2\sqrt{k_\phi^2+k_0^2}}{\hbar^2}(1+\sin 2\varphi)+\frac{\hbar^2\sqrt{k_\phi^2+k_0^2}}{2m^2}\left(4k_\phi^2+k_0^2-\frac{8m^2\lambda^2}{\hbar^4}\right)\sin 2\phi\sin 2\varphi\right]d\phi \\
&\approx \frac{\sqrt{m}e^2\tau\boldsymbol{\varepsilon}}{2\sqrt{2}\pi^2\hbar\sqrt{E_F+E_P}}\int_0^{2\pi}\left[\frac{\hbar^2}{m^2}\left(\frac{9}{2}k_0 k_\phi^2-\frac{4m^2\lambda^2 k_\phi^2}{\hbar^4 k_0}-\frac{8m^2\lambda^2 k_0}{\hbar^4}+k_0^3\right)\cos^2\phi+\frac{4\lambda^2}{\hbar^2}\left(k_0+\frac{k_\phi^2}{2k_0}\right)\sin 2\phi\right. \\
&\qquad\qquad \left. +\frac{2\lambda^2}{\hbar^2}\left(k_0+\frac{k_\phi^2}{2k_0}\right)(1+\sin 2\varphi)+\frac{\hbar^2}{2m^2}\left(\frac{9}{2}k_0 k_\phi^2-\frac{4m^2\lambda^2 k_\phi^2}{\hbar^4 k_0}-\frac{8m^2\lambda^2 k_0}{\hbar^4}+k_0^3\right)\sin 2\phi\sin 2\varphi\right]d\phi \\
&= \frac{e^2\tau\boldsymbol{\varepsilon}}{4\pi\hbar^2\sqrt{E_F+E_P}}\left[4E_F\sqrt{E_F}+5E_P\sqrt{E_F}-\frac{2E_P^2}{\sqrt{E_F}}+\left(\frac{2E_P^2}{\sqrt{E_F}}-\frac{E_P\sqrt{E_F}}{2}\right)\sin 2\varphi\right].
\end{aligned}
\tag{A4}
$$

[1] R. H. Silsbee, Spin–orbit induced coupling of charge current and spin polarization, J. Phys.: Condens. Matter **16**, R179 (2004).

[2] Y. Ando and M. Shiraishi, Spin to charge inter conversion phenomena in the interface and surface states, J. Phys. Soc. Jpn. **86**, 011001 (2017).

[3] N. Nagaosa, J. Sinova, S. Onoda, A. H. MacDonald, and N. P. Ong, Anomalous Hall effect, Rev. Mod. Phys. **82**, 1539 (2010).

[4] M. I. Dyakonov and V. I. Perel, Current-induced spin orientation of electrons in semiconductors, Phys. Lett. A **35**, 459 (1971).

[5] J. Sinova, S. O. Valenzuela, J. Wunderlich, C. H. Back, and T. Jungwirth, Spin Hall effects, Rev. Mod. Phys. **87**, 1213 (2015).

[6] *Spintronics Handbook: Spin Transport and Magnetism*, 2nd ed., edited by E. Y. Tsymbal and I. Žutić (CRC Press, Taylor & Francis Group, London, 2019).

[7] A. Matos-Abiague and J. Fabian, Tunneling Anomalous and Spin Hall Effects, Phys. Rev. Lett. **115**, 056602 (2015).

[8] M. Ye. Zhuravlev, A. Alexandrov, L. L. Tao, and E. Y. Tsymbal, Tunneling anomalous Hall effect in a ferroelectric tunnel junction, Appl. Phys. Lett. **113**, 172405 (2018).

[9] E. L. Ivchenko and G. E. Pikus, New photogalvanic effect in gyrotropic crystals, JETP Lett. **27**, 604 (1978).

[10] A. G. Aronov and Yu. B. Lyanda-Geller, Nuclear electric resonance and orientation of carrier spins by an electric field, JETP Lett. **50**, 431 (1989).

[11] A. G. Aronov, Yu. B. Lyanda-Geller, and G. E. Pikus, Spin polarization of electrons by an electric current, Sov. Phys. JETP **73**, 537 (1991).

[12] V. M. Edelstein, Spin polarization of conduction electrons induced by electric current in two-dimensional asymmetric electron systems, Solid State Commun. **73**, 233 (1990).

[13] A. Manchon, H. C. Koo, J. Nitta, S. M. Frolov, and R. A. Duine, New perspectives for Rashba spin–orbit coupling, Nat. Mater. **14**, 871 (2015).

[14] A. Soumyanarayanan, N. Reyren, A. Fert, and C. Panagopoulos, Emergent phenomena induced by spin-orbit coupling at surfaces and interfaces, Nature (London) **539**, 509 (2016).

[15] L. L. Tao, K. T. Cheung, L. Zhang, and J. Wang, All-electrical generation of spin-polarized currents in quantum spin Hall insulators, Phys. Rev. B **95**, 121407(R) (2017).

[16] L. L. Tao and E. Y. Tsymbal, Two-dimensional spin-valley locking spin valve, Phys. Rev. B **100**, 161110(R) (2019).

[17] L. L. Tao, A. Naeemi, and E. Y. Tsymbal, Valley-Spin Logic Gates, Phys. Rev. Appl. **13**, 054043 (2020).

[18] J. C. R. Sánchez, L. Vila, G. Desfonds, S. Gambarelli, J. P. Attané, J. M. De Teresa, C. Magén, and A. Fert, Spin-to-charge conversion using Rashba coupling at the interface between non-magnetic materials, Nat. Commun. **4**, 2944 (2013).

[19] H. J. Zhang, S. Yamamoto, B. Gu, H. Li, M. Maekawa, Y. Fukaya, and A. Kawasuso, Charge-to-Spin Conversion and Spin Diffusion in Bi/Ag Bilayers Observed by Spin-Polarized Positron Beam, Phys. Rev. Lett. **114**, 166602 (2015).

[20] A. R. Mellnik, J. S. Lee, A. Richardella, J. L. Grab, P. J. Mintun, M. H. Fischer, A. Vaezi, A. Manchon, E.-A. Kim, N. Samarth, and D. C. Ralph, Spin-transfer torque generated by a topological insulator, Nature (London) **511**, 449 (2014).

[21] C. H. Li, O. M. J. van't Erve, J. T. Robinson, Y. Liu, L. Li, and B. T. Jonker, Electrical detection of charge-current-induced spin polarization due to spin-momentum locking in Bi_2Se_3, Nat. Nanotechnol. **9**, 218 (2014).

[22] E. Lesne, Y. Fu, S. Oyarzun, J. C. Rojas-Sánchez, D. C. Vaz, H. Naganuma, G. Sicoli, J.-P. Attané, M. Jamet, E. Jacquet, J.-M. George, A. Barthélémy, H. Jaffrès, A. Fert, M. Bibes, and L. Vila, Highly efficient and tunable spin-to-charge conversion through Rashba coupling at oxide interfaces, Nat. Mater. **15**, 1261 (2016).

[23] Y. Wang, R. Ramaswamy, M. Motapothula, K. Narayanapillai, D. Zhu, J. Yu, T. Venkatesan, and H. Yang, Room-temperature giant charge-to-spin conversion at the $SrTiO_3-LaAlO_3$ oxide interface, Nano Lett. **17**, 7659 (2017).

[24] Q. Song, H. Zhang, T. Su, W. Yuan, Y. Chen, W. Xing, J. Shi, J. Sun, and W. Han, Observation of inverse Edelstein effect in Rashba-split 2DEG between $SrTiO_3$ and $LaAlO_3$ at room temperature, Sci. Adv. **3**, e1602312 (2017).

[25] T. S. Ghiasi, A. A. Kaverzin, P. J. Blah, and B. J. van Wees, Charge-to-Spin conversion by the Rashba−Edelstein effect in two-dimensional van der Waals heterostructures up to room temperature, Nano. Lett. **19**, 5959 (2019).

[26] C. Rinaldi, J. C. Rojas-Sánchez, R. N. Wang, Y. Fu, S. Oyarzun, L. Vila, S. Bertoli, M. Asa, L. Baldrati, M. Cantoni, J.-M. George, R. Calarco, A. Fert, and R. Bertacco, Evidence for spin to charge conversion in GeTe(111), APL Mater. **4**, 032501 (2016).

[27] P. Noël, F. Trier, L. M. V. Arche, J. Bréhin, D. C. Vaz, V. Garcia, S. Fusil, A. Barthélémy, L. Vila, M. Bibes, and J.-P. Attané, Non-volatile electric control of spin–charge conversion in a $SrTiO_3$ Rashba system, Nature (London) **580**, 483 (2020).

[28] R. H. Silsbee, Theory of the detection of current-induced spin polarization in a two-dimensional electron gas, Phys. Rev. B **63**, 155305 (2001).

[29] M. Trushin and J. Schliemann, Anisotropic current-induced spin accumulation in the two-dimensional electron gas with spin-orbit coupling, Phys. Rev. B **75**, 155323 (2007).

[30] M. Duckheim, D. Loss, M. Scheid, K. Richter, İ. Adagideli, and P. Jacquod, Spin accumulation in diffusive conductors with Rashba and Dresselhaus spin-orbit interaction, Phys. Rev. B **81**, 085303 (2010).

[31] P. Gambardella and I. M. Miron, Current-induced spin–orbit torques, Philos. Trans. R. Soc. A **369**, 3175 (2011).

[32] I. V. Tokatly, E. E. Krasovskii, and G. Vignale, Current-induced spin polarization at the surface of metallic films: A theorem and an *ab initio* calculation, Phys. Rev. B **91**, 035403 (2015).

[33] A. Johansson, J. Henk, and I. Mertig, Theoretical aspects of the Edelstein effect for anisotropic two-dimensional electron gas and topological insulators, Phys. Rev. B **93**, 195440 (2016).

[34] C. Gorini, A. Maleki Sheikhabadi, K. Shen, I. V. Tokatly, G. Vignale, and R. Raimondi, Theory of current-induced spin polarization in an electron gas, Phys. Rev. B **95**, 205424 (2017).

[35] J. M. Ziman, *Principles of the Theory of Solids* (Cambridge University Press, Cambridge, 1972).

[36] A. Manchon and S. Zhang, Theory of nonequilibrium intrinsic spin torque in a single nanomagnet, Phys. Rev. B **78**, 212405 (2008).

[37] L. L. Tao and E. Y. Tsymbal, Perspectives of spin-textured ferroelectrics, J. Phys. D **54**, 113001 (2021).

[38] S. Singh and A. H. Romero, Giant tunable Rashba spin splitting in a two-dimensional BiSb monolayer and in BiSb/AlN heterostructures, Phys. Rev. B **95**, 165444 (2017).

[39] K. Y. Mak, L. L. Tao, and Y. Zhou, Polarization tunable Rashba effect in 2D $LiAlTe_2$, Appl. Phys. Lett. **118**, 062404 (2021).

[40] L. L. Tao, T. R. Paudel, A. A. Kovalev, and E. Y. Tsymbal, Reversible spin texture in ferroelectric HfO_2, Phys. Rev. B **95**, 245141 (2017).

[41] M. Hirayama, R. Okugawa, S. Ishibashi, S. Murakami, and T. Miyake, Weyl Node and Spin Texture in Trigonal Tellurium and Selenium, Phys. Rev. Lett. **114**, 206401 (2015).

[42] M. Sakano, M. Hirayama, T. Takahashi, S. Akebi, M. Nakayama, K. Kuroda, K. Taguchi, T. Yoshikawa, K. Miyamoto, T. Okuda, K. Ono, H. Kumigashira, T. Ideue, Y. Iwasa, N. Mitsuishi, K. Ishizaka, S. Shin, T. Miyake, S. Murakami, T. Sasagawa, and T. Kondo, Radial Spin Texture in Elemental Tellurium with Chiral Crystal Structure, Phys. Rev. Lett. **124**, 136404 (2020).

[43] L. L. Tao and E. Y. Tsymbal, Persistent spin texture enforced by symmetry, Nat. Commun. **9**, 2763 (2018).

[44] M. Offidani, M. Milletarì, R. Raimondi, and A. Ferreira, Optimal Charge-to-Spin Conversion in Graphene on Transition-Metal Dichalcogenides, Phys. Rev. Lett. **119**, 196801 (2017).

[45] W. Lin, L. Li, F. Doğan, C. Li, H. Rotella, X. Yu, B. Zhang, Y. Li, W. S. Lew, S. Wang, W. Prellier, S. J. Pennycook, J. Chen, Z. Zhong, A. Manchon, and T. Wu, Interface-based tuning of Rashba spin-orbit interaction in asymmetric oxide heterostructures with 3d electrons, Nat. Commun. **10**, 3052 (2019).

[46] Sz. Vajna, E. Simon, A. Szilva, K. Palotas, B. Ujfalussy, and L. Szunyogh, Higher-order contributions to the Rashba-Bychkov effect with application to the Bi/Ag(111) surface alloy, Phys. Rev. B **85**, 075404 (2012).

[47] L. Fu, Hexagonal Warping Effects in the Surface States of the Topological Insulator Bi_2Te_3, Phys. Rev. Lett. **103**, 266801 (2009).

[48] Ł. Karwacki, A. Dyrdał, J. Berakdar, and J. Barnaś, Current-induced spin polarization in the isotropic k-cubed Rashba model: Theoretical study of p-doped semiconductor heterostructures and perovskite-oxide interfaces, Phys. Rev. B **97**, 235302 (2018).

[49] P. Schwab and R. Raimondi, Magnetoconductance of a two-dimensional metal in the presence of spin-orbit coupling, Eur. Phys. J. B **25**, 483 (2002).

[50] A. Dyrdał, J. Barnaś, and V. K. Dugaev, Current-induced spin polarization of a magnetized two-dimensional electron gas with Rashba spin-orbit interaction, Phys. Rev. B **95**, 245302 (2017).

[51] A. Manchon and S. Zhang, Theory of spin torque due to spin-orbit coupling, Phys. Rev. B **79**, 094422 (2009).

[52] A. Manchon, J. Železný, I. M. Miron, T. Jungwirth, J. Sinova, A. Thiaville, K. Garello, and P. Gambardella, Current-induced spin-orbit torques in ferromagnetic and antiferromagnetic systems, Rev. Mod. Phys. **91**, 035004 (2019).

[53] V. A. Sablikov and Y. Ya. Tkach, Van Hove scenario of anisotropic transport in a two-dimensional spin-orbit coupled electron gas in an in-plane magnetic field, Phys. Rev. B **99**, 035436 (2019).

[54] I. V. Kozlov and Yu. A. Kolesnichenko, Magnetic field driven topological transitions in the noncentrosymmetric energy spectrum of the two-dimensional electron gas with Rashba-Dresselhaus spin-orbit interaction, Phys. Rev. B **99**, 085129 (2019).

[55] L. L. Tao and E. Y. Tsymbal, Insulator-to-conductor transition driven by the Rashba-Zeeman effect, npj Comput. Mater. **6**, 172 (2020).

[56] K. Ishizaka, M. S. Bahramy, H. Murakawa, M. Sakano, T. Shimojima, T. Sonobe, K. Koizumi, S. Shin, H. Miyahara, A. Kimura, K. Miyamoto, T. Okuda, H. Namatame, M. Taniguchi, R. Arita, N. Nagaosa, K. Kobayashi, Y. Murakami, R. Kumai, Y. Kaneko, Y. Onose, and Y. Tokura, Giant Rashba-type spin splitting in bulk BiTeI, Nat. Mater. **10**, 521 (2011).

[57] D. Di Sante, P. Barone, R. Bertacco, and S. Picozzi, Electric control of the giant Rashba effect in bulk GeTe, Adv. Mater. **25**, 509 (2013).

[58] L. L. Tao and J. Wang, Strain-tunable ferroelectricity and its control of Rashba effect in $KTaO_3$, J. Appl. Phys. **120**, 234101 (2016).

[59] L. G. D. da Silveira, P. Barone, and S. Picozzi, Rashba-Dresselhaus spin-splitting in the bulk ferroelectric oxide $BiAlO_3$, Phys. Rev. B **93**, 245159 (2016).

[60] K. Tsutsui and S. Murakami, Spin-torque efficiency enhanced by Rashba spin splitting in three dimensions, Phys. Rev. B **86**, 115201 (2012).

[61] C. O. Avci, K. Garello, A. Ghosh, M. Gabureac, S. F. Alvarado, and P. Gambardella, Unidirectional spin Hall magnetoresistance in ferromagnet/normal metal bilayers, Nat. Phys. **11**, 570 (2015).

[62] K. Yasuda, A. Tsukazaki, R. Yoshimi, K. S. Takahashi, M. Kawasaki, and Y. Tokura, Large Unidirectional Magnetoresistance in a Magnetic Topological Insulator, Phys. Rev. Lett. **117**, 127202 (2016).

[63] Y. Fan, Q. Shao, L. Pan, X. Che, Q. He, G. Yin, C. Zheng, G. Yu, T. Nie, M. R. Masir, A. H. MacDonald, and K. L. Wang, Unidirectional magnetoresistance in modulation-doped magnetic topological insulators, Nano Lett. **19**, 692 (2019).